Automatic Delineation of the Myocardial Wall From CT Images Via Shape Segmentation and Variational Region Growing

Liangjia Zhu*, Yi Gao, Vikram Appia, Anthony Yezzi, Chesnal Arepalli, Tracy Faber, Arthur Stillman, and Allen Tannenbaum, *Fellow, IEEE*

***Abstract*—Prognosis and diagnosis of cardiac diseases frequently require quantitative evaluation of the ventricle volume, mass, and ejection fraction. The delineation of the myocardial wall is involved in all of these evaluations, which is a challenging task due to large variations in myocardial shapes and image quality. In this paper, we present an automatic method for extracting the myocardial wall of the left and right ventricles from cardiac CT images. In the method, the left and right ventricles are located sequentially, in which each ventricle is detected by first identifying the endocardium and then segmenting the epicardium. To this end, the endocardium is localized by utilizing its geometric features obtained on-line from a CT image. After that, a variational region-growing model is employed to extract the epicardium of the ventricles. In particular, the location of the endocardium of the left ventricle is determined via using an active contour model on the blood-pool surface. To localize the right ventricle, the active contour model is applied on a heart surface extracted based on the left ventricle segmentation result. The robustness and accuracy of the proposed approach is demonstrated by experimental results from 33 human and 12 pig CT images.**

***Index Terms*—Left ventricle (LV), myocardial wall segmentation, right ventricle (RV), salient component, shape segmentation, variational region growing.**

I. Introduction

DELINEATING the myocardial wall of the left (LV) and right (RV) ventricles is an important step in the prognosis and diagnosis of cardiac diseases. This topic has been investigated for decades [1], and it is still an active research field [2]–[4]. The main challenges include wide shape variability between different cardiac cycles and between different patients, weak edges between epicardium and heart fat or soft tissues, and thin thickness of the RV wall.

Model-based methods have become dominant in this research [1] to get an accurate and robust segmentation. Typically, a heart model is built by learning the geometric or intensity features of the heart from cardiac images. While in segmentation, a commonly used framework is first globally aligning the model to an image and then deforming this model to fit image content. Global localization is achieved by detecting the geometric or intensity features of the heart. Local deformations are performed by optimizing an objective function defined between the model parameters and image features. In particular, the model-based methods can be roughly categorized based on whether these models are applied explicitly or implicitly for segmentation. In the first type of methods, typically a heart surface model is fitted to images for segmentation. For example, in active shape models (ASMs) [5], [6], a statistical shape model called the point distribution model is learned from a set of aligned shapes using the principal component analysis (PCA) technique, which is then iteratively aligned to image boundaries. Active appearance models (AAMs) extend this idea by incorporating gray level information [7] and were used in segmenting the left and right ventricles from MR images [8]. The deformations allowed in the parametric models such as ASMs and AAMs are restricted to the shape space where the heart models are embedded. A more sophisticated way of representing the shape space is by using 3-D diffusion wavelets [9], which encode shape variations hierarchically. Using deformable models, the authors in [10] and [11] provided a way to incorporate shape priors that allows adaptivity for local variations. In these methods, an annotated heart surface model is deformed to match image content by optimizing affine or similarity transformations defined between the model parameters and image features. In particular, landmark

Manuscript received December 22, 2012; revised May 18, 2013; March 18, 2013; accepted May 22, 2013. Date of publication June 4, 2013; date of current version September 14, 2013. This work was supported in part by the grants from the NIH, AFOSR, ARO, ONR, and MDA, in part by the National Alliance for Medical Image Computing, funded by the National Institutes of Health through the NIH Roadmap for Medical Research under Grant U54 EB005149 (information on the National Centers for Biomedical Computing can be obtained from http://nihroadmap.nih.gov/bioinformatics), in part by the National Center for Research Resources under Grant P41-RR-013218, in part by the National Institute of Biomedical Imaging and Bioengineering under Grant P41-EB-015902 of the National Institutes of Health, and in part by the NIH under Grant R01 HL085417. T. Faber receives royalties from the sale of the Emory Cardiac Toolbox and has an equity position in Syntermed, Inc., which markets ECTb. The terms of this arrangement have been reviewed and approved by Emory University in accordance with its conflict of interest policies. *Asterisk indicates corresponding author.*

*L. Zhu is with the School of Electrical and Computer Engineering, Georgia Institute of Technology, Atlanta, GA 30303 USA (e-mail: lzhu@gatech.edu).

Y. Gao is with the Psychiatry Neuroimaging Laboratory, Harvard Medical School, Boston, MA 02115 USA (e-mail: gaoyi@bwh.harvard.edu).

V. Appia and A. Yezzi are with the School of Electrical and Computer Engineering, Georgia Institute of Technology, Atlanta, GA 30303 USA (e-mail: vikram.appia@gatech.edu; ayezzi@ece.gatech.edu).

C. Arepalli, T. Faber, and A. Stillman are with the Department of Radiology, Emory University, Atlanta, GA 30322 USA (e-mail: carepal@emory.edu; tfaber@emory.edu; aestill@emory.edu).

A. Tannenbaum is with the Comprehensive Cancer Center/ECE, UAB, Birmingham, AL 35294 USA (e-mail: arobertan@gmail.com).

Color versions of one or more of the figures in this paper are available online at http://ieeexplore.ieee.org.

Digital Object Identifier 10.1109/TBME.2013.2266118

0018-9294 © 2013 IEEE

points on the interventricular septum were used to guide the segmentation in [11]. Instead of deforming a prealigned model, atlas-based methods use shape information implicitly by directly registering atlas image to a target image. Then, either the labels from multiple atlases are fused [12] or registered atlases are deformed [13] to extract the heart chambers. However, the segmentation of the myocardial wall of the RV has been neglected in these state-of-the-art model-based methods [10], [11], [13]. Model-free methods are also widely used to explore the characteristics of heart geometry or intensity distribution from other perspectives. For example, the random forests method was used to model the geometric and intensity features in the myocardial region for delineating the myocardium [14]. For a comprehensive literature review of heart segmentation, see [1] and [2] and references therein.

How to localize the model initially is a less studied topic, especially for these methods using deformable models, which tend to get stuck in undesirable local extrema when started without a good initialization. Typically, the geometric features of the heart are used for localization. For example, in [15], the LV endocardium was initialized by searching for a circular structure in a blood pool mask obtained via thresholding. A similar empirical rule was used in identifying the left ventricle cavity [16]. Examples of more advanced localization methods include the generalized Hough transform [10] and optimization of similarity transformation for a heart model [11]. Atlas-based registration has also been used for coarse initialization [9], [13].

One observation that may be utilized for the localization is that the ventricles are salient components on the heart surface. This is where the shape decomposition/segmentation technique can be utilized to cluster the surface into *meaningful* components based on some given criteria as in computer graphics and geometric modeling [17], [18]. For example, a surface may be hierarchically decomposed into regions of deep concavities by using fuzzy clustering and graph partition techniques [19]. Applications of shape segmentation in medical imaging can be found in heart modeling from images [20] and aneurysm neck detection on vessel surfaces [21]. Active contour models have also been applied on surfaces to refine coarse segmentations [22] or extract objects of interest [23]. The Shape segmentation technique would be a powerful tool for ventricle localization because ventricles are prominent components on the heart surface. Among the few applications of this technique in cardiac image segmentation, the *narrowing* of vessels around the left atrium was detected by merging local features based on given criteria to extract the left atrium [24].

In this paper, we propose a method for automatically extracting the myocardial wall from cardiac CT images, which integrates region growing with shape segmentation in a natural way. In this framework, the shape segmentation provides seed regions for region growing while the latter reconstructs a heart surface for the shape segmentation. Specifically, the segmentation process starts by localizing the LV endocardium. Unlike the localization methods described so far, our method is based on the observation that the LV is a salient component on the blood pool surface, which can be identified on the surface by utilizing shape segmentation techniques. After that, a variational region-growing method [25], driven by the robust statistics of a seed region around the endocardium is applied to localize the epicardium. Once the LV is determined, the RV is localized based on the segmentation of the LV. The RV epicardium is initialized in the same way as in localizing the LV epicardium. Finally, these myocardial surfaces are refined by employing an active contour model using the initial segmentations as a constraint.

The contributions of the proposed method are as follows:

1) we present an automatic localization method for both ventricles with high accuracy. Unlike other methods that only use low level information from voxels, our method captures a global geometric characteristic of the ventricles. Hence, it is not sensitive to such issues as variability in ventricle shapes and volume coverages. Note that, as an initialization step, this localization method can be easily incorporated into other model-based frameworks.
2) The proposed method is able to segment thin-layer structures like the myocardium of the RV, which has been neglected by some of these latest methods [10], [11], [13].
3) The overall system is complete in that all the active contour models involved are initialized automatically and robustly, other than in those systems where active contours are either used as a single component or initialized manually. In addition, no training image is required in our method, which works in the cases where the number of images available is limited.

The rest of this paper is organized as follows. In Section II, we describe the details of the overall framework, including the localization of the ventricles and wall structure extraction. In Section III, we provide some experimental results to demonstrate the robustness and accuracy of the proposed method. Finally, in Section IV, we draw some conclusions and outline some future research directions.

II. Proposed Method

The flowchart of the proposed method is shown in Fig. 1. The overall segmentation process consists of ventricle localization and myocardial wall extraction. First, the LV is localized by using shape segmentation techniques. Then, the RV is identified on a heart surface constructed based on the segmentation of the LV. Finally, the myocardial wall, lying between the epicardial and endocardial surfaces of the ventricles, is refined by employing an active contour model with a constraint based on the localization results. The main steps are described in the following sections.

A. Localize the LV

Assume that the orientation of a CT image is given and there is sufficient contrast between blood pool and myocardium. The localization of the LV is determined via searching for a deep concave boundary on the blood pool surface as follows.

1) Extract Blood Pool Surface: Since CT images have calibrated gray levels, the source image is thresholded to highlight the blood pool region. Then, a morphological opening operator is applied to remove noisy arteries and cut spines that may be residing in the same connected component of the heart. The

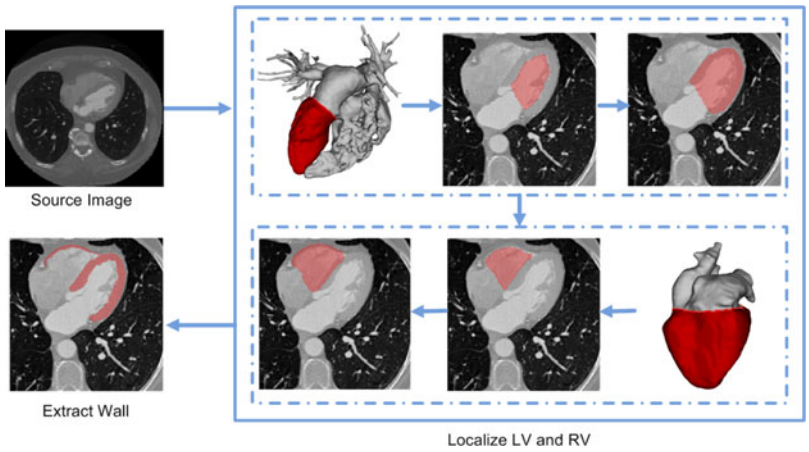

Fig. 1. Flowchart of the proposed approach.

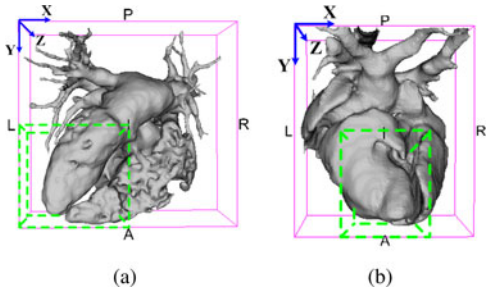

Fig. 2. Orientation of (a) human and (b) pig blood pool surfaces in the source image coordinate system. The reference directions are left(L), right(R), posterior(P), anterior(A), inferior(I), and superior(S). The ROIs are highlighted in green.

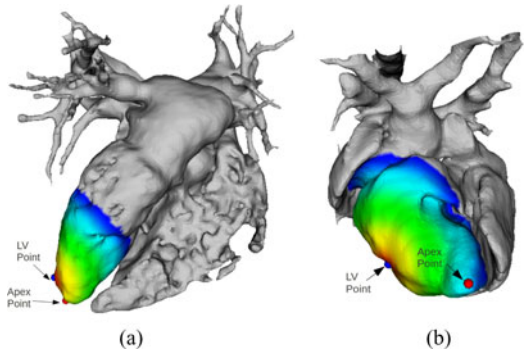

Fig. 3. Apex detection of (a) human and (b) pig hearts. The color map shows the distance field within $N(p_{\mathrm{lv}})$.

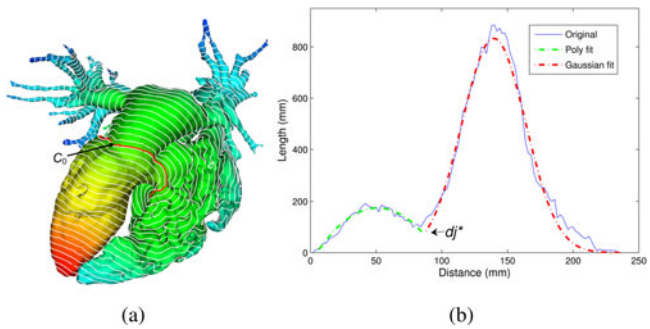

Fig. 4. Detection of the initial cut contour. (a) Distance field from the apex with isocontours. The initial cut contour C_0 is marked in red. (b) Length of isocontours versus distance, and the determination of the optimal d_{j^*}.

largest connected component is chosen and triangulated as the blood pool surface.

2) Detect Apex Point: Suppose the coordinate system of the source image is left–posterior–inferior (LPI) as shown in Fig. 2. The anatomy of the pig heart is almost identical to human's but with a different long-axis orientation [26]. As shown in the figure, the long axis of the human heart is pointing toward the anterior plane, while the pig's is tilted in the inferior direction. Thus, to narrow down the search space, the left-most point in a predefined region of interest (ROI) is first determined. Then, a neighborhood of this point is explored so that it is large enough to cover the apex point. After that, the most anterior and inferior points within the neighborhood $N(p_{\mathrm{lv}})$ are selected as the human and pig apex points, respectively. See Fig. 3. A human data point will be used to demonstrate the rest of the steps.

3) Find an Initial Cut Contour: An initial cut contour, denoted by C^0_{lv}, can be found by analyzing the distance field starting from the apex point. As can be seen from Fig. 4, the lengths of isocontours on the distance field increase gradually, and then drop slightly. After a certain point, they are growing rapidly followed by sharp reductions. An explanation of this pattern is that the LV has an overall ellipsoid-like shape, which is concave around the base area. Thus, the total length of an isocontour at distance d may be modeled as

$$h(d,\tilde{d}) = \begin{cases} c_0 + c_1 d + c_2 d^2 & \text{if } d \le \tilde{d} \\ a e^{-\frac{(d-\mu)^2}{2\sigma^2}} & \text{if } d > \tilde{d} \end{cases} \quad (1)$$

where the first equation captures the behavior as the isocontours travel on the LV, and the second one models this relation when the isocontours propagate further away; here, $\tilde{d}$ serves as a turning point for these two modes. Let (d_i, l_i), $i = 1 \ldots n$, be a pair consisting of a sampled distance and its corresponding isocontour length, where n is the number of samples over the

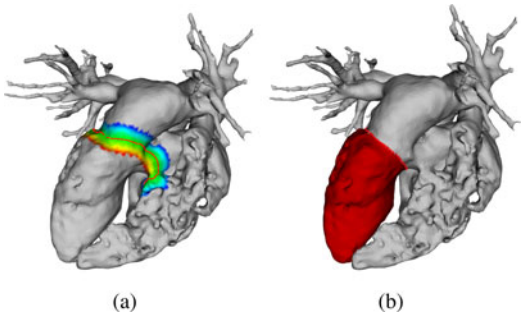

(a) (b)

Fig. 5. LV localization. (a) Initial contour $C_{\rm lv}^0$ and its narrow band. (b) Segmented endocardial surface.

distance field. Then, the initial cut contour is approximated by searching for the optimal turning point d_{j^*}, where j^* minimizes the least-squares fitting error.

$$j^* = arg\min_j \left(arg \min_{c_0,c_1,c_2} \sum_{i=1}^{j} (h(d_i,d_j) - l_i)^2 + arg \min_{a,\mu,\sigma} \sum_{i=j+1}^{n} (\log h(d_i,d_j) - \log l_i)^2 \right). \quad (2)$$

Here, d_j is a sample point serving as a trial turning point. The optimal turning point d_{j^*} is obtained by exhausting all the elements in $\{d_j\}, j = 1 \ldots n$.

4) Refine the Cut Contour: The geometric active contour model [27], [28] is used to refine the initial cut contour $C_{\rm lv}^0$. Suppose a contour on the blood pool surface $M_{\rm bp}$ is represented by the zero level set of a function $U : M_{\rm bp} \to \mathbb{R}$ with $U(C(p,t)) = 0$, where $C(p,t)$ is a family of contours on $M_{\rm bp}$. Let $g : M_{\rm bp} \to \mathbb{R}^+$ be a positive function that attracts an active contour to a conceptually desired boundary [22].

$$g(p) = \frac{1}{1 + (|\kappa(p)|/S)^2} \quad (3)$$

where $\kappa(p)$ is the mean curvature at p, and S is a constant for scales that was empirically set as $S = 0.01$. As in [22], κ is set to zero if it is positive. The geometric active contour model on the surface $M_{\rm bp}$ is defined as

$$E(U) = \int_{M_{\rm bp}} g(p)\delta(U(p))|\nabla_{M_{\rm bp}} U(p)|dp \quad (4)$$

where $\delta(U)$ is the Dirac delta function. The energy $E(U)$ evaluates a weighted contour length. Gradient descent technique is employed to solve (4). See the Appendix for details.

To reduce the effect of local noise, the contour evolution process described previously may be applied twice. In the first round, set $g = 1$ so that it shortens the initial contour by the geodesic curvature flow. Then, the feature function defined in (3) is utilized to refine the contour so that it stops at expected locations. An illustration of the LV localization process is shown in Fig. 5.

5) Extract the LV Endocardium: The endocardial surface $M_{\rm endo}^{\rm lv}$ is closed by triangulating the points along the cut contour $C_{\rm lv}$, which is rasterized to get a mask image $\tilde{I}_{\rm endo}^{\rm lv}$. To remove noise and papillary muscles, the morphological closing operator is applied inside the convex hull of the endocardial surface. An example of papillary muscle removal is shown in Fig. 6.

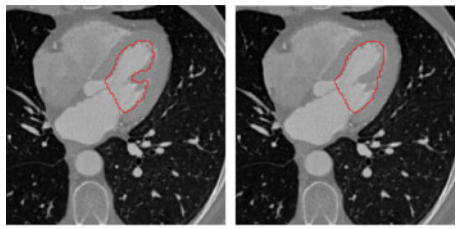

(a) (b)

Fig. 6. Segmentation of the endocardium (red) (a) before and (b) after removing the papillary muscles.

6) Segment the LV Epicardium: One way of initializing the epicardium mask is by dilating the endocardium to a given distance. For example, the elements of $\tilde{I}_{\rm epi}^{\rm lv}$ may be determined by choosing voxels within a certain distance range to the $\tilde{I}_{\rm endo}^{\rm lv}$ boundary. This works well for a myocardial wall with a nearly uniform thickness. Here, another way is proposed to initialize $\tilde{I}_{\rm epi}^{\rm lv}$ by utilizing a variational region-growing method that is driven by the robust statistics of image intensities. Similar to dilation-based methods, a distance field from $\tilde{I}_{\rm endo}^{\rm lv}$ is computed and a small strip region lying between $d_{\rm in}$ and $d_{\rm out}$ is chosen as the seed region for the epicardium mask. Typically, the values are set to $d_{\rm in} = 2$ mm and $d_{\rm out} = 4$ mm. The blood pool voxels are excluded from this region. Once the seed region is determined, the robust-statistics-based energy functional [25] is then defined as

$$E_{\rm RS}(\phi) = \lambda_{\rm RS} \int_\Omega -p(\boldsymbol{f}(x))H(\phi(x))dx + (1-\lambda_{\rm RS}) \int_\Omega \delta(x)|\nabla\phi(x)|dx \quad (5)$$

where ϕ is the signed distance function from the epicardium mask and H is the Heaviside function. Here, $p(\boldsymbol{f}(x))$ is the probability density function of a feature vector $\boldsymbol{f}(x)$ that evaluates the intensity median, interquartile range, and median absolute deviation, respectively, around a neighborhood of a point $x \in \Omega$. This probability function $p(\boldsymbol{f}(x))$ can be learned from the intensities inside the seed region via kernel regression. The first term in this equation measures the intensity homogeneity inside the contour, and the second term is the length of the contour that controls the smoothness of the final result. In practice, $\lambda_{\rm RS}$ was set as $\lambda_{\rm RS} = 0.2$.

The myocardial masks, $\tilde{I}_{\rm epi}^{\rm lv}$ and $\tilde{I}_{\rm end}^{\rm lv}$, provide a good localization of the epicardium and endocardium, which impose a shape constraint for local refinement, especially on regions of low contrast or poor edges.

B. Localize the RV

The same strategy is used to localize the RV as follows.

1) Reconstruct the Heart Surface: The intensity inside the RV blood pool may not be as homogeneous as the LV. To identify the RV, a smooth heart surface is first reconstructed by taking

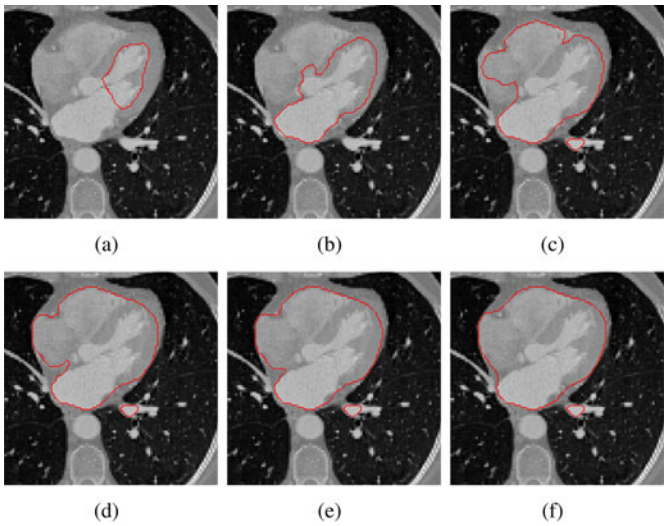

Fig. 7. Variational region-growing process for segmenting the heart surface.

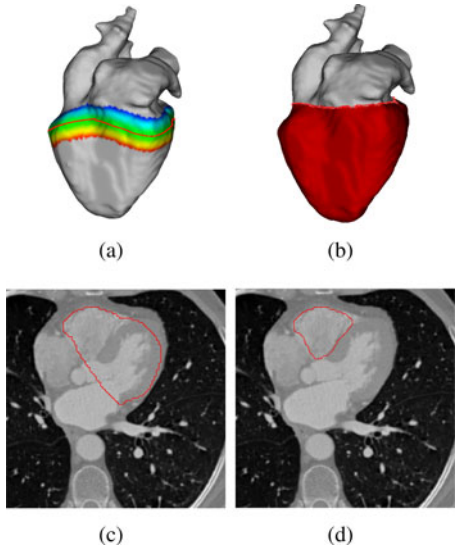

Fig. 8. Segmentation of the RV endocardium. (a) Initial contour $C^0_{\rm rv}$ and its narrow band. (b) Ventricles (red) determined by $C_{\rm lv}$ on the heart surface $M_{\rm ht}$. (c) Ventricles in the source image. (d) RV endocardium.

the LV endocardium as a seed region to start the variational region-growing process defined in (5). In implementation, the parameter $\lambda_{\rm RS}$ was set as $\lambda_{\rm RS} = 0.9$ so that the intensity homogeneity force term plays a leading role while competing with the smoothing force to explore the entire heart region. The surface is represented as a triangulated surface, denoted by $M_{\rm ht}$. An example of the region-growing process is shown in Fig. 7. Since the blood pool occupies the majority of the LV endocardial mask, the growing process shows a higher tendency to expand brighter regions than the darker ones. Combining the effect of the smoothing term, the growing process gradually captures a smooth heart region.

2) Find an Initial Cut Contour: The closest point from $M_{\rm ht}$ to the LV apex $p_{\rm apx}$ is used as a starting point to reconstruct the distance field on $M_{\rm ht}$. Then, the distance field is sampled evenly at an interval of 2 mm. Let $\{\tilde{p}_i\}, i = 1 \cdots m$, be the points of a given isocontour C. The distance between the isocontour and the cut contour $C_{\rm lv}$ of $M_{\rm bp}$ is approximated by

$$d(C, C_{\rm lv}) = \frac{1}{m}\sum_{i=1}^{m} |\mathbf{N}_{\rm lv} \cdot (\tilde{p}_i - p_c)| \tag{6}$$

where $\mathbf{N}_{\rm lv}$ and p_c are the unit normal of the best fitting plane and centroid of $C_{\rm lv}$, respectively. Then, the isocontour with the minimal distance to $C_{\rm lv}$ is selected as the initial contour that identifies the ventricles on $M_{\rm ht}$.

3) Segment the RV Endocardium: The initial cut contour $C^0_{\rm vs}$ is refined by using the geometric active contour model described in Section II-A4. The surface determined by $C_{\rm vs}$ includes both the LV and RV, which is rasterized to get a mask for the ventricles, denoted by $\tilde{I}_{\rm vs}$. The RV endocardium mask is obtained by removing the LV and blood pool voxels from $\tilde{I}_{\rm vs}$. Fig. 8 shows the process of segmenting the RV endocardium.

4) Segment the RV Epicardium: The same procedure as in Section II-A6 is applied to generate the RV epicardium mask $\tilde{I}^{\rm rv}_{\rm epi}$.

C. Extract the Myocardial Wall

To extract the myocardial wall, the mask images of the ventricles are refined by employing an active contour method with a shape constraint that allows local variations around the segmented masks. After that, the outlier voxels are excluded to get a complete wall structure.

1) Refine the Myocardial Masks: Given a mask image $\tilde{I} \in \{\tilde{I}^{\rm lv}_{\rm endo}, \tilde{I}^{\rm rv}_{\rm endo}, \tilde{I}^{\rm lv}_{\rm epi}, \tilde{I}^{\rm rv}_{\rm epi}\}$ of a myocardial surface, the energy functional for refinement is designed as

$$E(\phi) = \lambda \int_{\Omega_x} \delta(\phi(x)) \int_{\Omega_y} B(x,y) F(I(y), \phi(y)) dy dx + (1-\lambda) \int_{\Omega} \tilde{g}(\tilde{\phi}(x)) \delta(x) |\nabla \phi(x)| dx \tag{7}$$

where $B(x, y)$ is a ball centered at x with radius r, $F(I(y), \phi(y))$ is a generic internal energy term defined over Ω, and $\tilde{g}$ is a modified Sigmoid function to rescale the signed distance function $\tilde{\phi}$ of $\tilde{I}$.

$$\tilde{g}(\tilde{\phi}) = (d_{\max} - d_{\min})\Big(1 + \exp\Big(\frac{-|\tilde{\phi}| - \beta}{\alpha}\Big)\Big)^{-1} + d_{\min}. \tag{8}$$

Here, $d_{\min}$ and $d_{\max}$ control the range of the signed distance, α and β determine the shape of the function. Typically, we set $\alpha = 1, \beta = 5, d_{\min} = 0.02$ mm and $d_{\max} = 1.0$ mm. The first term in (7) is a localized region-based energy [29]. In this study, the Chan–Vese energy [30] is used for $F(I(y), \phi(y))$. The second term is essentially the geometric active contour energy [27], [28] using the feature image $\tilde{g}$ to allow local deformations around the initial contour.

2) Extract the Myocardial Wall: The myocardial wall is defined as the volume between the endocardium and epicardium masks. The majority of the wall can be determined by performing the logic XOR operation between the endocardium and epicardium masks of the LV and RV, respectively. Note that

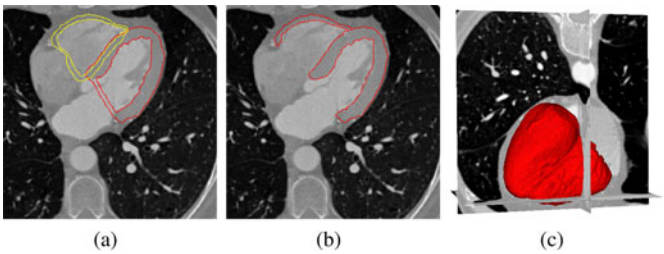

Fig. 9. Segmentation of the myocardial wall. (a) Refined myocardial masks. (b) Extracted myocardial wall. (c) Wall in 3-D view.

the contour evolution process returns closed surfaces. Thus, the voxels inside the blood pool are excluded to extract a complete myocardial wall. An example of extracting the myocardial wall is given in Fig. 9.

III. Experimental Results

This study was approved by the Institutional Review Board. We tested the robustness and accuracy of the proposed method using 33 human and 12 pig cardiac CT images. The data include anomaly cases (hypertrophic cardiomyopathy and aneurysm) and volumes with different scanning quality.

A. Implementation

The overall framework was implemented in C++. Open source packages ITK [31] and VTK [32] were used for basic image processing tasks and 3-D visualization, respectively.

In extracting the blood pool, the source image was down-sampled to a voxel resolution of 2.0 mm $\times$ 2.0 mm $\times$ 2.0 mm. The shape of the LV is well preserved at this resolution. The thresholds of 180 and 350 in Hounsfield units were used for the human and pig datasets, respectively, so that the ventricles can be separated after thresholding.

In detecting the apex point, the ROI for the human data was set as a rectangular box located at the left–anterior–inferior corner, which is one-eighth of the size of its corresponding bounding box of M_{bp}. The ROI for the pig data was defined similarly but centered in the left-to-right direction. The neighborhood size $N(p_{\mathrm{lv}})$ is controlled by a threshold, which was empirically set as 50 mm.

To find the isocontour length model, the distance field was sampled evenly at an interval of 2 mm. In refining the cut contour, the size of the narrow band is controlled by a threshold $\phi_{\max}$, which is typically set as $\phi_{\max} = \min(10, 4l_{\max})$ mm, where $l_{\max}$ is the length of the longest edge on M_{bp}. The time step $dt = 1$ was used in implementation.

To remove the papillary muscles, the structure element size depends on that of the papillary muscles, which was empirically set as 3 mm. To extract the LV epicardium, a parameter d_w is used to control the maximum distance allowed in the region-growing process. The value of this parameter is related to the maximal thickness of the myocardial wall, which typically ranges from 6 to 16 mm [2]. Thus, d_w was set as $d_w = 16$ mm. For the RV epicardium, typically, the seed region is controlled by $d_{\mathrm{out}} = 2$ mm and $d_{\mathrm{out}} = 3$ mm, and set $d_w = 5$ mm.

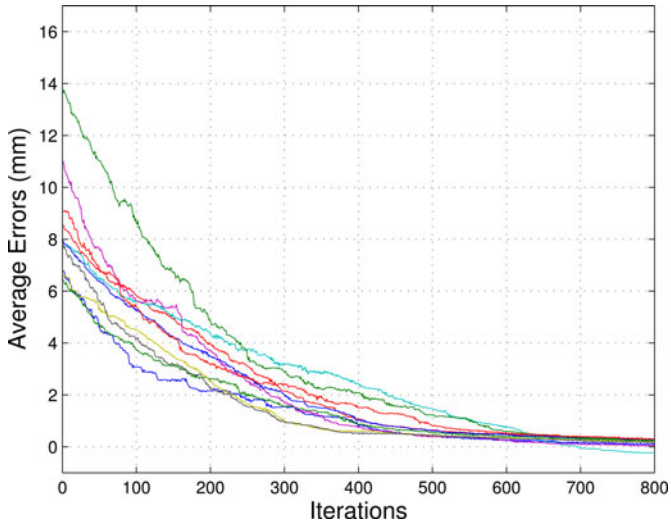

Fig. 10. Evolution of cut contours generated from ten randomly sampled apex points.

The sparse level set method [33] was utilized to implement gradient descent flows derived from the active contour models in (5) and (7) for its efficiency. In particular, the upwind scheme was used in discretizing $|\nabla(\cdot)|$ (see [34] for details). The endocardium and epicardium masks were refined separately. The radius of the ball $B(x, y)$ was set as $r = 4$ mm.

B. Robustness Test

Locating the LV is a key step in the overall framework. To test the robustness of this step, sample points randomly selected from a neighborhood within 30 mm of the apex point were used as trial apex points to start the localization process. To quantify errors, the distance between the cut contours obtained using different sample points and the original contour was measured as

$$\mathrm{Dist}(C, \tilde{C}) = \frac{\int_{\tilde{C}(s)} D(C) ds}{\int_{\tilde{C}(s)} ds}. \tag{9}$$

Here, $C, \tilde{C}$, and D are the original cut contour, the cut contour obtained from a sample point, and the distance between them, respectively. In our implementation, $D(C)$ was evaluated at triangle vertices. The evolution process of $\mathrm{Dist}(C, \tilde{C})$ for 10 sample points is shown in Fig. 10. All of the curves converge to the original C within a tolerable numerical error. In addition, the averages of the turning point $\tilde{d}$ are 94 ± 9 mm and 76 ± 6 mm for the human and pig data, respectively. This shows that the feature used for identifying the cut contour is stable despite of the variability in heart shapes.

Our method succeeded in localizing the LV and RV for all of the testing data with wide shape variations and different volume coverages. Typical segmentation results returned by the proposed method are shown in Fig. 11 displayed with manual segmentations. The first row is a normal human case with small field of view (FOV) and the second is a pig case with wide FOV.

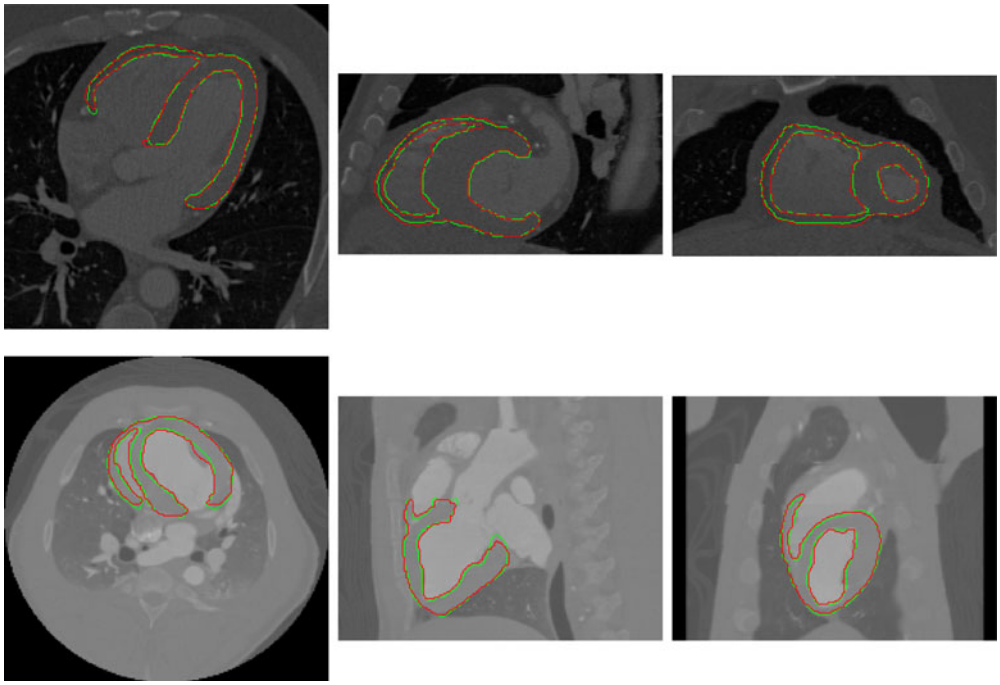

Fig. 11. Comparison of automatic (red) and manual (green) segmentations of normal cases from human (top row) and pig (second row) data. From left to right are myocardial wall in axial, coronal, and sagittal views, respectively.

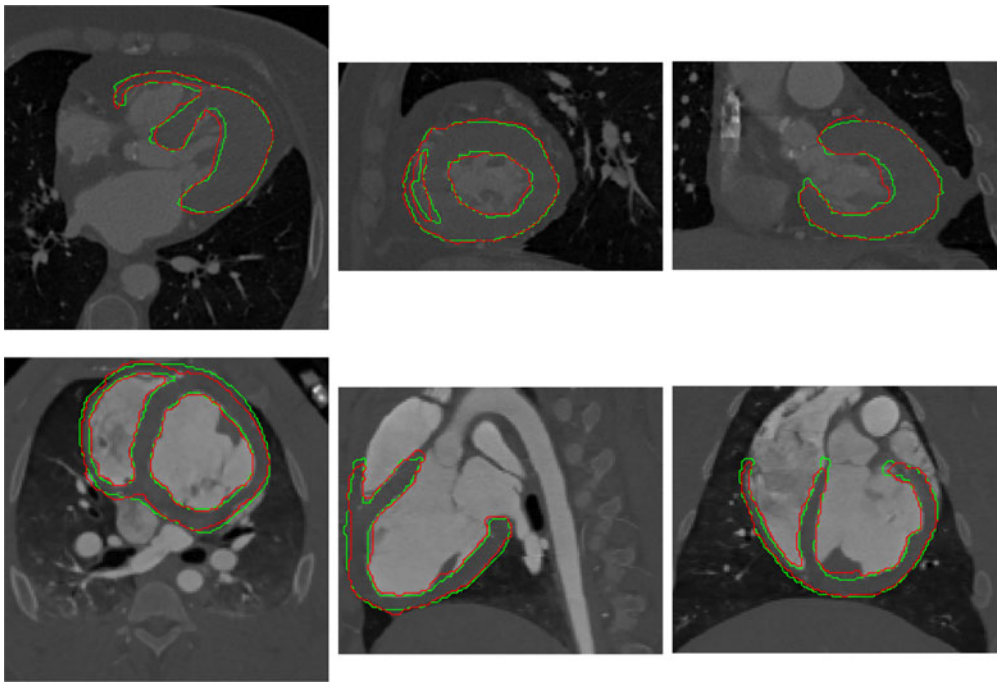

Fig. 12. Comparison results of challenging cases from automatic (red) and manual (green) segmentations. Top: human case with hypertrophic cardiomyopathy; Bottom: pig case with papillary muscles and low SNR boundaries (the middle bottom figure). From left to right are the myocardial wall in axial, coronal, and sagittal views, respectively.

Fig. 12 shows results from challenging cases. The first row is for a human case with hypertrophic cardiomyopathy, and the second is for a pig case with large papillary muscles and low SNR boundaries around the pericardium. As can be seen from these results, the papillary muscles and soft tissues were successfully excluded from the myocardium.

C. Quantitative Analysis

The segmentation results from the proposed method were validated by two doctors who were blind to the method. One doctor delineated the human dataset, the other did the pig dataset. To make a fair comparison, all testing datasets were resampled to the same resolution of the manual segmentations at

TABLE I
MEAN AND STANDARD DEVIATION OF THE POINT-TO-SURFACE ERRORS IN LOCALIZATION AND REFINEMENT (IN MM)

Data	Stages	LV-Endo	LV-Epi	RV-Endo	RV-Epi
Human	Localization	1.06 ± 1.01	1.27 ± 1.24	1.70 ± 1.95	2.00 ± 2.05
	Refinement	0.87 ± 0.94	1.06 ± 1.15	1.51 ± 1.80	1.60 ± 1.90
Pig	Localization	0.83 ± 0.89	1.05 ± 1.12	1.31 ± 1.43	1.78 ± 1.70
	Refinement	0.72 ± 0.88	0.80 ± 0.99	1.28 ± 1.40	1.32 ± 1.64

TABLE II
COMPARISON BETWEEN THE PROPOSED METHOD AND LOCALIZED PCA FOR THE SEGMENTATION OF PIG VENTRICLES(IN MM)

Method	LV-Endo	LV-Epi	RV-Endo	RV-Epi
Proposed method	0.72 ± 0.88	0.80 ± 0.99	1.28 ± 1.40	1.32 ± 1.64
Local-PCA	1.08 ± 1.12	1.10 ± 1.40	1.58 ± 1.71	1.61 ± 1.96

1.0 mm $\times$ 1.0 mm $\times$ 1.0 mm. The mean and standard deviation of the point-to-surface errors for the human and pig datasets at the localization and refinement steps are summarized in Table I. These results demonstrate that the localization step locates the endocardium and epicardium masks with high precision as compared to the manual segmentations, which are further refined by applying the active contour model with the shape constraint. Note that the accuracy of the endocardium segmentation is better than the epicardium segmentation as the former is better defined due to the higher contrast between the blood pool and the myocardium, while in the latter case, poor contrast and weak edges are present between the epicardium and background tissues.

In addition, the proposed method was compared to a state-of-the-art active contour method, i.e., the localized PCA-based method [35], [36], for segmenting pig ventricles using the same dataset. The point-to-surface errors are summarized in Table II. In addition, the statistical differences between these two methods were analyzed by utilizing the two-sample *t*-test, with null hypothesis as "the PCA-based method has a smaller mean error than the proposed method," for LV-Endo, LV-Epi, RV-Endo, and RV-Epi. The test rejects the null hypothesis at the 1% significance level for all of the four cases. As indicated by these results, the proposed method statistically has a higher accuracy for segmenting both ventricles as it captures more local image content than the PCA-based method, which relies on the subspace where the heart shape is embedded.

Though it is hard to make a fair comparison between different methods for human ventricle segmentation by using different datasets, the accuracy of the proposed method seems to be competitive with some latest results: 1.13 ± 0.55 and 1.21 ± 0.41 mm [11], 0.98 ± 1.32 and 0.82 ± 1.07 mm [10] for LV endocardium and epicardium, respectively. Note that, the comparison was only made to the LV segmentation because the approaches being compared model the RV endocardium and epicardium as a single component.

IV. CONCLUSION AND FUTURE RESEARCH

We have presented an automatic method for segmenting the ventricles from cardiac CT images. The method sequentially segments the LV and RV via integrating shape segmentation with region-growing techniques. In particular, each ventricle is detected by first identifying the endocardium and then segmenting the epicardium. In addition, the LV segmentation results are used to localize the RV. The local variations of the heart are naturally handled by utilizing features obtained online. Its performance has been evaluated by measuring the errors between automatic and manual segmentations. In these tests, the proposed method achieves high accuracy as well as strong robustness for segmenting the myocardial wall from both human and pig datasets with large shape variabilities and different volume coverages. In future work, we plan to apply the segmentations from the proposed approach to clinical applications such as evaluating the myocardial mass at risk caused by stenoses.

APPENDIX

GEOMETRIC ACTIVE CONTOURS ON SURFACES

The gradient descent flow for solving (4) is

$$\begin{cases} \dfrac{\partial U}{\partial t} = |\nabla_{M_{\rm bp}} U| \nabla_{M_{\rm bp}} \cdot \left(g(p) \dfrac{\nabla_{M_{\rm bp}} U}{|\nabla_{M_{\rm bp}} U|} \right) \\ \dfrac{\partial U}{\partial \overrightarrow{n}}|_{\partial M_{\rm bp}} = 0 \\ U(0) = U(C_{\rm lv}^0) \end{cases} \tag{10}$$

where $\partial M_{\rm bp}$ is the boundary of $M_{\rm bp}$ and $\overrightarrow{n}$ is the intrinsic outward normal of $\partial M_{\rm bp}$. Here, $\nabla_{M_{\rm bp}}$ is the del operator on $M_{\rm bp}$. A narrow band method is applied to implement the gradient flow. Specifically, U is realized as the signed distance function from $C_{\rm lv}^0$, which decomposes $M_{\rm bp}$ into several regions. The sign of U is positive in the region that contains the apex point.

Algorithm Narrow band for the Geometric Active Contour

1: Initialize the level set function U with C_{lv}^0
2: Construct a narrow band $\Omega_{M_{bp}}$ around the current contour on M_{bp}
3: Update U in $\Omega_{M_{bp}}$, according to

$$U(p,t+1) = U(p,t) + dt \left(|\nabla_{M_{bp}} U| \nabla_{M_{bp}} \cdot \left(g \frac{\nabla_{M_{bp}} U}{|\nabla_{M_{bp}} U|} \right) \right)_{(p,t)}, \tag{11}$$

where dt is the time step in discretizing U
4: Find the new zero level set of U to update the contour C
5: Repeat steps 2-4 until it converges or reaches the maximum number of iterations

The key step is to numerically approximate the gradient and divergence operators on a surface. The discretization schemes of [23] were adopted as they naturally capture the geometric properties of surfaces.

ACKNOWLEDGMENT

We especially wish to acknowledge our deep gratitude to Dr. Faber who had helped to push this research forward and devoted her life to cardiac image analysis. We would also like to thank Dr. Ernest Garcia of Emory from some useful discussions about the topic of this paper.

REFERENCES

[1] J. S. Suri, "Computer vision, pattern recognition and image processing in left ventricle segmentation: The last 50 years," *Pattern Anal. Appl.*, vol. 3, no. 3, pp. 209–242, 2000.

[2] C. Petitjean and J. N. Dacher, "A review of segmentation methods in short axis cardiac MR images," *Med. Image Anal.*, vol. 15, no. 2, pp. 169–184, 2011.

[3] (2009). MICCAI Workshop—Cardiac MR Left Ventricle Segmentation Challenge, [Online]. Available: http://smial.sri.utoronto.ca/LV_Challenge/Home.html

[4] (2012). MICCAI Workshop—3D Cardiovascular Imaging Segmentation Challenge, [Online]. Available: http://grand-challenge2012.bigr.nl/

[5] T. F. Cootes, C. J. Taylor, D. H. Cooper, and J. Graham, "Active shape models-their training and application," *Comput. Vis. Image Understand.*, vol. 61, no. 1, pp. 38–59, 1995.

[6] D. Fritz, R. Unterhinninghofen, R. Dillmann, D. Rinck, and M. Scheuering, "Automatic segmentation of the left ventricle and computation of diagnostic parameters using region growing and a statistical model," in *Proc. SPIE Med. Imag.*, 2005, vol. 5747, pp. 1844–1854.

[7] T. F. Cootes, G. J. Edwards, and C. J. Taylor, "Active appearance models," *IEEE Trans. Pattern Anal. Mach. Intell.*, vol. 23, no. 6, pp. 681–685, Jun. 2001.

[8] S. C. Mitchell, B. Lelieveldt, R. J. van der Geest, J. G. Bosch, J. H. C. Reiber, and M. Sonka, "Multistage hybrid active appearance model matching: Segmentation of left and right ventricles in cardiac MR images," *IEEE Trans. Med. Imag.*, vol. 20, no. 5, pp. 415–423, 2001.

[9] S. Essafi, G. Langs, and N. Paragios, "Hierarchical 3D diffusion wavelet shape priors," in *Proc. Int. Conf. Comput. Vis.*, 2009, pp. 1717–1724.

[10] O. Ecabert, J. Peters, H. Schramm, C. Lorenz, J. von Berg, M. Walker, M. Vembar, M. E. Olszewski, K. Subramanyan, G. Lavi, and J. Weese, "Automatic model-based segmentation of the heart in CT images," *IEEE Trans. Med. Imag.*, vol. 27, no. 9, pp. 1189–1201, Sep. 2008.

[11] Y. Zheng, A. Barbu, B. Georgescu, M. Scheuering, and D. Comaniciu, "Four-chamber heart modeling and automatic segmentation for 3D cardiac CT volumes using marginal space learning and steerable features," *IEEE Trans. Med. Imag.*, vol. 27, no. 11, pp. 1668–1681, Nov. 2008.

[12] E. M. van Rikxoort, I. Isgum, Y. Arzhaeva, M. Staring, S. Klein, M. A. Viergever, J. P. W. Pluim, and B. van Ginneken, "Adaptive local multi-atlas segmentation: Application to the heart and the caudate nucleus," *Med. Image Anal.*, vol. 14, no. 1, pp. 39–49, 2010.

[13] X. Zhuang, K. S. Rhode, R. R., D. J. Hawkes, and S. Ourselin, "A registration-based propagation framework for automatic whole heart segmentation of cardiac MRI," *IEEE Trans. Med. Imag.*, vol. 29, no. 9, pp. 1612–1625, Sep. 2010.

[14] V. S. Lempitsky, M. Verhoek, J. A. Noble, and A. Blake, "Random forest classification for automatic delineation of myocardium in real-time 3D echocardiography," in *Proc. 5th Int. Conf. Funct. Imag. Model. Heart*, 2009, pp. 447–456.

[15] M. Jolly, "Automatic segmentation of the left ventricle in cardiac MR and CT images," *Int. J. Comput. Vis.*, vol. 70, no. 2, pp. 151–163, 2006.

[16] M. Lynch, O. Ghita, and P. Whelan, "Automatic segmentation of the left ventricle cavity and myocardium in MRI data," *Comput. Biol. Med.*, vol. 36, no. 4, pp. 389–407, Apr. 2006.

[17] A. Shamir, "A survey on mesh segmentation techniques," *Comput. Graph. Forum*, vol. 27, no. 6, pp. 1539–1556, 2008.

[18] M. Attene, S. Katz, M. Mortara, G. Patanè, M. Spagnuolo, and A. Tal, "Mesh segmentation—A comparative study," in *Proc. IEEE Int. Conf. Shape Model. Appl.*, 2006, pp. 14–25.

[19] S. Katz and A. Tal, "Hierarchical mesh decomposition using fuzzy clustering and cuts," *ACM Trans. Graph.*, vol. 22, no. 3, pp. 954–961, Jul. 2003.

[20] C. Bajaj, S. Goswami, Z. Yu, Y. Zhang, Y. Bazilevs, and T. Hughes, "Patient specific heart models from high resolution CT," in *Proc. Int. Symp. Comput. Model. Objects Represent. Images: Fund., Methods, Appl.*, 2006.

[21] R. Cárdenes, J. Pozo, H. Bogunovic, I. Larrabide, and A. Frangi, "Automatic aneurysm neck detection using surface voronoi diagrams," *IEEE Trans. Med. Imag.*, vol. 30, no. 10, pp. 1863–1876, Oct. 2011.

[22] L. Kaplansky and A. Tal, "Mesh segmentation refinement," *Pacif. Graph.*, vol. 28, no. 7, pp. 1995–2003, 2009.

[23] R. Lai and T. F. Chan, "A framework for intrinsic image processing on surfaces," *Comput. Vis. Image Understand.*, vol. 115, no. 12, pp. 1647–1661, 2011.

[24] M. John and N. Rahn, "Automatic left atrium segmentation by cutting the blood pool at narrowings," in *Medical Image Computing and Computer-Assisted Intervention* (Lecture notes in Computer Science). Berlin, Germany: Springer, 2005, pp. 798–805.

[25] Y. Gao, R. Kikinis, S. Bouix, M. Shenton, and A. Tannenbaum, "A 3D interactive multi-object segmentation tool using local robust statistics driven active contours," *Med. Image Anal.*, vol. 16, no. 6, pp. 1216–1227, 2012.

[26] S. J. Crick, M. N. Sheppard, S. Y. Ho, L. Gebstein, and R. H. Anderson, "Anatomy of the pig heart: comparisons with normal human cardiac structure," *J. Anatomy*, vol. 193, pp. 105–119, 1998.

[27] S. Kichenassamy, A. Kumar, P. Olver, A. Tannenbaum, and A. Yezzi, "Conformal curvature flows: From phase transitions to active contours," *Arch. Rational Mech. Anal.*, vol. 134, pp. 275–301, 1996.

[28] V. Caselles, R. Kimmel, and G. Sapiro, "Geodesic active contours," *Int. J. Comput. Vis.*, vol. 22, no. 1, pp. 61–79, 1997.

[29] S. Lankton and A. Tannenbaum, "Localizing region-based active contours," *IEEE Trans. Image Process.*, vol. 17, no. 11, pp. 2029–2039, Nov. 2008.

[30] T. F. Chan and L. A. Vese, "Active contours without edges," *IEEE Trans. Image Process.*, vol. 10, no. 2, pp. 2029–2039, Feb. 2001.

[31] Insight Segmentation and Registration Toolkit (ITK), [Online]. Available: http://www.itk.org/

[32] Visualization Toolkit (VTK), [Online]. Available:http://www.vtk.org/

[33] R. T. Whitaker, "A level-set approach to 3D reconstruction from range data," *Int. J. Comput. Vis.*, vol. 29, no. 3, pp. 203–231, Sep. 1998.

[34] G. Aubert and P. Kornprobst, *Mathematical Problems in Image Processing: Partial Differential Equations and the Calculus of Variations* (Applied Mathematical Sciences). New York, NY, USA: Springer-Verlag, 2006.

[35] V. Appia, B. Ganapathy, A. Abufadel, A. Yezzi, and T. Faber, "A regions of confidence based approach to enhance segmentation with shape priors," in *Proc. SPIE Med. Imag.*, 2010, pp. 753302-1–753302-12.

[36] V. Appia, B. Ganapathy, A. Yezzi, and T. Faber, "Localized principal component analysis based curve evolution: A divide and conquer approach," in *Proc. IEEE Int. Conf. Comput. Vis.*, 2011, pp. 1981–1986.

Authors' photographs and biographies not available at the time of publication.